RSC Advances

PAPER

View Article Online
View Journal | View Issue

Cite this: *RSC Adv.*, 2020, **10**, 13302

The implementation of artificial neural networks for the multivariable optimization of mesoporous NiO nanocrystalline: biodiesel application

Soroush Soltani, *[a] Taha Roodbar Shojaei,[b] Nasrin Khanian,[c] Thomas Shean Yaw Choong,[a] Umer Rashid,[d] Imededdine Arbi Nehdi[ef] and Rozita Binti Yusoff[g]

In the present research, artificial neural network (ANN) modelling was utilized to determine the relative importance of effective variables to achieve optimum specific surface areas of a synthesized catalyst. Initially, carbonaceous nanocrystalline mesoporous NiO core–shell solid sphere composites were produced by applying incomplete carbonized glucose (ICG) as the pore directing agent and polyethylene glycol (PEG; 4000) as the surfactant *via* a hydrothermal-assisted method. The Brunauer–Emmett–Teller (BET) model was applied to ascertain the textural characteristics of the as-prepared mesoporous NiO catalyst. The effects of several key parameters such as metal ratio, surfactant and template concentrations, and calcination temperature on the prediction of the surface areas of the as-synthesized catalyst were evaluated. In order to verify the optimum hydrothermal fabrication conditions, ANN was trained over five different algorithms (QP, BBP, IBP, LM, and GA). Among five different algorithms, LM-4-7-1 representing 4 nodes in the input layer, 7 nodes in the hidden layer, and 1 node in the output layer was verified as the optimum model due to its optimum numerical properties. According to the modelling study, the calcination temperature demonstrated the most effective parameter, while the ICG concentration indicated the least effect. By verifying the optimum hydrothermal fabrication conditions, the thermal decomposition of ammonium sulphate (TDAS) was applied to the functionalized surface areas and mesoporous walls by $-SO_3H$ functional groups. In addition, the catalytic performance and reusability of the produced mesoporous SO_3H–NiO catalyst were evaluated *via* the transesterification of waste cooking palm oil, resulting in a methyl ester content of 97.4% and excellent stability for nine consecutive transesterification reactions without additional treatments.

Received 30th January 2020
Accepted 26th February 2020

DOI: 10.1039/d0ra00892c

rsc.li/rsc-advances

Introduction

The huge consumption of conventional diesel fuel has caused the rapid exhaustion of petroleum resources. Besides, the threat of climate change and environmental pollution due to the emission of hazardous greenhouse gases is the one of the most critical issues across the world. Among alternative possible sources, biodiesel has prompted intense interest as a capable substitute for current fuel.

The most favourable approaches of biodiesel production are the conventional esterification of free fatty acids (FFAs) or the transesterification of triglycerides (TG) along with alcohol over a proper base/acid catalyst. Recent advances in reusable solid acid catalysts are being paid great attention in many chemical reactions such as esterification, transesterification, hydrolysis, and hydration. This class of catalysts, containing both Lewis and Brønsted types, has been proposed as an alternative to the un-reusable homogeneous acid/base catalysts. In contrast with homogeneous base/acid catalysts, heterogeneous acid catalysts possess a number of advantages such as easy separation from the reaction medium, eradication of washing procedure, and minimization of corrosion. Hydrophobicity is another merit of heterogeneous acid catalysts, which prevents the access of polar by-products to a majority of the active sites. It is noteworthy to mention that the distribution of polar reagents into the exterior active surface of the catalyst may cause the de-activation of the catalyst.[1] In addition, these type of catalysts can be merely recovered and reused, which considerably diminish the rate of

[a]*Department of Chemical and Environmental Engineering, Universiti Putra Malaysia, 43400 Selangor, Malaysia. E-mail: soroush.soltaani@gmail.com*

[b]*Department of Mechanical Engineering of Agricultural Machinery, Faculty of Agricultural Engineering and Technology, College of Agriculture and Natural Resources, University of Tehran, Karaj, Iran*

[c]*Department of Physics, Faculty of Science, Islamic Azad University, Karaj, Iran*

[d]*Institute of Advanced Technology, Universiti Putra Malaysia, 43400 Selangor, Malaysia*

[e]*Department of Chemistry, College of Science, King Saud University, Riyadh 11451, Saudi Arabia*

[f]*Laboratoire de Recherche LR18ES08, Chemistry Department, Science College, Tunis El Manar University, Tunis 2092, Tunisia*

[g]*Department of Chemical Engineering, Faculty of Engineering, University of Malaya, W. Persekutuan Kuala Lumpur, 50603 Kuala Lumpur, Malaysia*

fabrication.[2] As a result, the environment friendly heterogeneous acid catalysts are likely to be swapped with ecologically unfavourable homogeneous acid catalysts.

Moreover, conventional heterogeneous acid catalysts have lost their position in inorganic syntheses because of their poor structural, physicochemical, and textural properties that limit the reach of the reagents to the active sites through catalytic reactions. In this case, synthesizing novel mesoporous catalysts with a high specific surface area (S_{BET}) and flexible and homogeneous pore diameters (D_p) have attracted the most attention in inorganic syntheses. In general, the fabrication of mesostructured materials can be done through templating approaches in the presence of a surfactant.[3,4] Nevertheless, there are several key parameters such as metal ratio, surfactant and template concentrations, and annealing temperature that influence the S_{BET} of the synthesized catalyst.[5] However, it is quite difficult to estimate the relative importance of these critical parameters on the specific surface areas of the synthesized catalyst. Therefore, well-known multi-variate semi-empirical approaches such as response surface methodology (RSM) and artificial neural networks (ANNs) can be applied to optimize the possible relative condition.[6–9]

The RSM projects the related conditions, fits the detected practical outcomes of the executed model at that point, and then proposes the most suitable model for further authentication. In this method, the confirmed model is typically applied to gain the maximum yield of the final product. However, the modelling process involves some complex numerical calculations such as fitting and the reversion process. On the other hand, the ANN modelling is free of any complications due to high reliability in obtaining non-linear association amongst the input and output variables.[10–12] Unlike RSM, the ANN modelling is not funded on mathematical models and can be simply applied for simulation of such a complex system.[13–16] Through ANN modelling, the output is typically generated after accumulation of input data *via* processing of the fundamental elements. On the other hand, the output is identified upon learning from a sequence of cases without knowing about the relation between them.[17–19] However, the main challenge is to verify a suitable algorithm among various algorithms [quick propagation (QP), Levenberg–Marquardt (LM), genetic algorithm (GA), incremental back-propagation (IBP), and batch back-propagation (BBP)] through the learning procedure.[20] Through the process, the weights and biases should improve to simultaneously lessen the inaccuracies and enhance the capability of the method. Subsequently, the miscalculation value is determined between the predicted and real output data.[21,22]

Furthermore, ANN as a non-linear statistical analysis technique has been vastly applied in various nanotechnology applications.[6,23–27] Generally, it is considered as a promising simulation technique, which hugely diminish the rate of fabrication by predicting the output results with a short level of error in the prediction.

In this research work, the carbonaceous mesoporous NiO core–shell solid sphere composites were produced using incomplete carbonized glucose (ICG) as the pore directing agent and polyethylene glycol (PEG; 4000) as the surfactant *via* hydrothermal assisted method. The effect of different hydrothermal reactions such as metal ratio, surfactant and template concentrations, and calcination temperature on the prediction of the surface areas of the synthesized catalyst were modelled by ANN. Afterwards, the thermal decomposition of ammonium sulphate (TDAS) was applied to enrich the surface areas and mesopore walls with $-SO_3H$ functional groups. It is known that introducing hydrophobic organic species *via* post-synthetic approaches results in severe lessening of the textural properties. The reduction of porosity and surface area could be assigned to the growth of functional species into the mesopore channels as the exterior and interior surface areas were drastically improved in the presence of hydrophobic species. By having this knowledge, the effect of only the hydrothermal parameters was evaluated and post-sulfonation treatment was only applied to maximize the functionality of the catalyst through transesterification reaction. Furthermore, the catalytic activity and reusability of the produced mesoporous SO_3H–NiO-ICG catalyst were determined *via* transesterification of waste cooking palm oil (WCPO).

Materials and methods

Materials

The analytical chemicals polyethylene glycol [PEG, $M_n = 4000$ g mol^{-1}], nickel nitrate [$Ni(NO_3)_2 \cdot 6H_2O$], and methanol (CH_3OH; ≥99.5%) were acquired from Fisher Scientific. D-Glucose ($C_6H_{12}O_6$), ammonium sulphate [$(NH_4)_2SO_4$; ≥99.5%], and urea [$CO(NH_2)_2$] were acquired from Sigma-Aldrich. The basic methyl esters for gas chromatography (GC) analysis (heptadecanoate, methyl-myristate, methyl-stearate, methyl-linoleate, methyl-palmitate, and methyl-oleate) were delivered by Fluka, USA.

The WCPO [holding 17.0% FFAs, acid value of 34.0 mg KOH per g, saponification value of 171.0 mg KOH per g, density (15 °C) of 0.91 g cm^{-3}, and kinematic viscosity (40 °C) of 33.0 mm^2 s^{-1}] was obtained from a local market, Malaysia. The supplied WCPO contained five most important FFAs including myristic acid (C14:0, 2.70%), stearic acid (C18:0, 7.13%), linoleic acid (C18:2, 12.59%), palmitic acid (C16:0, 34.80%), and oleic acid (C18:1, 42.78%).

Synthesis of the mesoporous SO_3H–NiO-ICG catalyst

Synthesis of mesoporous NiO-ICG catalyst. In this study, mesoporous NiO-ICG catalysts were synthesized hydrothermally in the presence of PEG as the surfactant and ICG as the template, as per our previous study.[28] Initially, 10 g of D-glucose was placed into a muffle furnace tube where the pyrolysis process took place in the presence of N_2 gas flow (at the rate of 100 mL min^{-1}) at 400 °C for 12 h. The synthesized powder was milled at 1000 rpm for 1 h and pounded to develop a uniformly fine ICG powder.

The autoclave-assisted system was used to fabricate a polymeric mesoporous NiO-ICG catalyst where nickel nitrate (2 g), PEG (10 g), urea (5 mmol), and ICG : Ni (5 : 1) were mixed into 150 mL deionized water under constant stirring. Next, the Teflon-lined stainless-steel autoclave was taped up and sustained at

200 °C for 18 h under autogenous-pressure. Afterwards, post-calcination at 600 °C for 4 h in the presence of N_2 gas flow took part to get rid of any kind of outstanding components as a result of the initial decomposition of the materials.

Post-functionalization through TDAS. The as-synthesized material was further treated by TDAS to improve the hydrophobic character of the catalyst by growing the aromatic groups and lessening the aliphatic rings. Here, 2 g of the as-prepared NiO-ICG nanocrystalline was added to 50 mL of ammonium sulphate and sonicated for 60 min. Afterwards, the blend was transferred into an autoclave, which was taped up and sustained at 200 °C for half an hour under autogenous-pressure. The prepared product was rigorously cleaned with a blend of deionized water and ethyl alcohol to diminish the unreacted components attached to the catalyst. Next, the product was dried up in an electric vacuum oven at 100 °C for 24 h. Ultimately, post-annealing treatment took place at 600 °C for 4 h in the presence of N_2 gas flow to diminish the residual volatiles and to fully activate the mesoporous SO_3H–NiO-ICG catalyst.

Catalyst characterization

The evaluation of the textural properties of the produced mesoporous NiO-ICG nanocrystalline material was performed using the Brunauer–Emmett–Teller (BET; Thermo Finnigan apparatus) model. The specific surface areas (S_{BET}) were determined by adsorption–desorption isotherm method while the pore distribution diameters were evaluated by Barrett–Joyner–Halenda (BJH) method. Prior to analysis, the catalyst went through pre-treatment to eliminate moisture and was degassed at 150 °C for 120 min over H_2 flow, and later the catalyst was submerged into a gassy vessel of N_2 with the temperature of −196 °C. At the end, the adsorption of N_2 was computed at the relative pressure.

To determine the acidity of the active sites, ammonia temperature-programmed desorption (NH_3-TPD; Thermo Finnigan TPDRO 1100) was introduced. Initially, a certain amount of mesoporous catalyst (0.4 g) was first treated with Ar gas at 150 °C and later, it was subjected to a frequent flow of NH_3 for 60 min. Finally, the adsorption of NH_3 was measured and computed along with heating the catalyst up to 900 °C with a thermal conductivity detector (TCD) while the rate of heating system was 15°C min^{-1} in 50 mL min^{-1} He gas.

X-ray diffraction (XRD; 6000 Shimadzu) was utilized to assess the physical and structural characteristics of the produced nanocrystalline material.

The microscopic morphology of NiO-ICG was characterized using transmission electron microscopy (TEM, Hitachi H-7100) and field emission scanning electron microscopy (FESEM, FEI Novanano 240) fitted with an energy dispersive X-ray (EDX) spectrometer (DMAX microscope at 200 kV).

The ANN modelling and learning procedure

In the process of ANN modelling, there are three majors layer including input, hidden, and output; each single layer contains several nodes that are typically linked by either multilayer feedback or feed-forward connection equation. In this case, the nodes of certain layers can be correlated to the nodes of the subsequent layers. In general, the characteristics of the biological neural networks can be simulated by artificial neurons (nodes). In this procedure, the data of input layer's nodes with special weight will be transformed to the hidden layer and then the output layer's nodes. The simulation is fulfilled *via* related weights throughout learning progression by well-known learning algorithms.[29]

During this study, a multilayer feed-forwards neural network (NN) was applied *via* five well-known common learning systems including quick propagation (QP), batch back propagation (BBP), incremental back propagation (IBP), Levenberg–Marquardt (LM), and genetic algorithm (GA).[30,31] Series of reactions were conducted to evaluate the impact of hydrothermal reaction factors on the textural properties. The inputs are metal ratio, surfactant and template concentrations, and calcination temperature while the output is the specific surface area. Over the synthetic procedure, one parameter was varying and the other three parameters were kept constant. All the tentative data utilized for ANN modelling using NeuralPower software version 2.5 and are reviewed in Table 1. The test, training, and authentication outputs were selected randomly by using RSM.

Throughout the learning procedure, the hidden layer and the output of the j^{th} in the output-layer is calculated through eqn (1):

$$y_i = \sum_{j=1}^{i} x_i w_{ij} + b_j \quad (1)$$

whereas, y_i is the input of the system to j node in the hidden layer, i is the nodes' numbers, b is the bias terms, x_i is the output of the ex-layer, and w_{ij} is the influence of linking between the i^{th} node and j^{th} node.

However, the main challenge is to minimize the errors by verifying the proper summation of interconnection weights through the training process.[32] It is highly essential to assess the prediction ability of the ANN simulation system. The root means square error (RMSE) is known as a unique assessment equation which is calculated by eqn (2):[33]

$$\mathrm{RMSE} = \left(1/n \sum_{i=1}^{n} (y_i - y_{di})^2\right)^{1/2} \quad (2)$$

where n is the sum of the points, y_i is the anticipated amount, and y_{di} is the actual amount.

It should be noted that the learning process keeps repeating to avoid casual connotation between the weights. The factor of determination (R^2) imitates the fit rate for the numerical pattern, which is calculated *via* eqn (3):[34]

$$R^2 = 1 - \sum_{i=1}^{n} (y_i - y_{di})^2 \Big/ \sum_{i=1}^{n} (y_{di} - y_m)^2 \quad (3)$$

where, y_m is the average of the actual values.

The absolute average deviation (AAD) is one more critical factor that commonly introduced us to assess the errors between actual and predicted values. The ADD is calculated by eqn (4):[17]

Table 1 Experimental outputs (training, testing, and validation), actual, and predicated values of specific surface area of the synthesized nanocrystalline NiO-ICG composites

Run no.	ICG con.	PEG con.	Ni con. (mmol)	Calcination temp. (°C)	Actual surface area ($m^2\ g^{-1}$)	Predicted surface area ($m^2\ g^{-1}$)
Training data set						
1	10	6	2	500	295	294.81
2	15	6	2	500	307	306.91
3	10	18	2	500	315	315.83
4	15	18	2	500	327	326.41
5	5	24	2	500	315	314.91
6	10	24	2	500	325	324.92
7	20	24	2	500	332	332.04
8	10	6	4	500	320	319.88
9	20	6	4	500	324	323.82
10	5	12	4	500	308	307.77
11	15	12	4	500	326	327.59
12	20	12	4	500	321	320.94
13	10	18	4	500	326	325.75
14	15	18	4	500	338	336.59
15	5	24	4	500	328	327.88
16	10	24	4	500	335	334.61
17	20	24	4	500	341	340.99
18	5	6	6	500	322	321.63
19	15	6	6	500	341	341.75
20	20	6	6	500	335	335.05
21	5	18	6	500	327	328.01
22	10	18	6	500	335	334.25
23	20	18	6	500	342	342.58
24	5	24	6	500	333	333.25
25	5	6	8	500	331	331.31
26	10	6	8	500	338	337.75
27	20	6	8	500	343	342.3
28	5	18	8	500	344	343.1
29	15	18	8	500	358	359.2
30	20	18	8	500	353	352.85
31	10	24	8	500	357	357.77
32	15	24	8	500	369	367.74
33	5	6	2	600	291	291.12
34	10	6	4	600	329	328.42
35	20	6	8	600	350	350.14
36	10	12	4	600	324	323.79
37	10	18	4	600	333	334.22
38	15	18	6	600	355	353.69
39	5	24	2	600	321	320.94
40	15	24	6	600	357	357.48
41	10	6	4	700	316	316.35
42	15	6	6	700	337	337.04
Training data set						
43	10	12	4	700	311	310.21
44	5	18	2	700	302	301.89
45	15	18	6	700	338	338.2
46	20	18	8	700	347	348.4
47	15	24	6	700	341	340.96
48	20	24	8	700	358	356.52
49	15	6	6	800	333	332.78
50	20	6	8	800	332	332.83
51	10	12	4	800	307	307.46
52	20	12	8	800	336	334.36
53	10	18	4	800	315	314.74
54	5	24	2	800	287	287.06
55	20	24	8	800	350	350.95
Test data set						
56	15	24	2	500	336	284.3

Table 1 (*Contd.*)

Run no.	ICG con.	PEG con.	Ni con. (mmol)	Calcination temp. (°C)	Actual surface area ($m^2\ g^{-1}$)	Predicted surface area ($m^2\ g^{-1}$)
57	15	6	4	500	330	306.39
58	10	12	4	500	317	319.13
59	5	18	4	500	319	337.13
60	20	18	4	500	333	331.17
61	15	24	4	500	344	315.92
62	10	6	6	500	330	319.29
63	5	12	6	500	315	329.42
64	10	18	8	500	349	346.23
65	5	24	8	500	350	329.33
66	20	24	8	500	364	320.89
67	15	6	6	600	348	347.47
68	5	18	2	600	314	339.49
69	20	18	8	600	360	350.01
70	10	18	4	700	320	348.23
71	5	24	2	700	297	351.5
72	10	6	4	800	310	364.68
73	5	12	2	800	286	349.47
74	5	18	2	800	297	318.09
75	15	24	6	800	334	360.61
Validation data set						
76	5	6	2	500	280	284.3
77	5	18	2	500	308	306.39
78	20	18	2	500	322	319.13
79	15	18	6	500	346	347.47
80	10	24	6	500	339	339.49
81	15	6	8	500	347	350.01
82	20	24	8	600	370	368.36
83	20	6	8	700	338	336.32

$$\mathrm{AAD} = \frac{1}{n}\sum_{i=1}^{n}|y_i - y_{di}|/y_{di} \quad (4)$$

It is known that the greatest NN model should possess the least RMSE value and maximum AAD and R^2 values.[35]

Transesterification procedure and characterization

Prior to the reaction, WCPO was pre-treated (at 120 °C for 20 min and then filtered) to get rid of moisture and other remainders. The autoclave-assisted transesterification of WCPO was performed to evaluate the catalytic activity and recyclability of SO_3H–NiO-ICG over the optimized conditions: the mesoporous catalyst amount of 1 wt%, methanol to WCPO molar ratio of 9 : 1, operating temperature of 100 °C and a mixing intensity of 450 rpm. By the end of every single reaction, the blend was centrifuged, residual methanol was vaporized, and later, the remaining mixture was located in a splitting funnel to separate glycerol from the produced ester.

The content of produced fatty acid methyl ester (FAME) was further determined by gas chromatography flame ionization detector (GC-FID; Agilent 7890A) whereas methyl heptadecanoate was used as an internal standard and methyl-myristate, methyl-stearate, methyl-linoleate, methyl-palmitate, and methyl-oleate were employed as the orientation standards. The content of produced methyl ester was calculated by the EN 14103 standard method *via* eqn (5):

$$C = \sum A \times \sum A_{meh}/A_{meh} \times C_{meh} \times V_{meh}/W_t \times 100\% \quad (5)$$

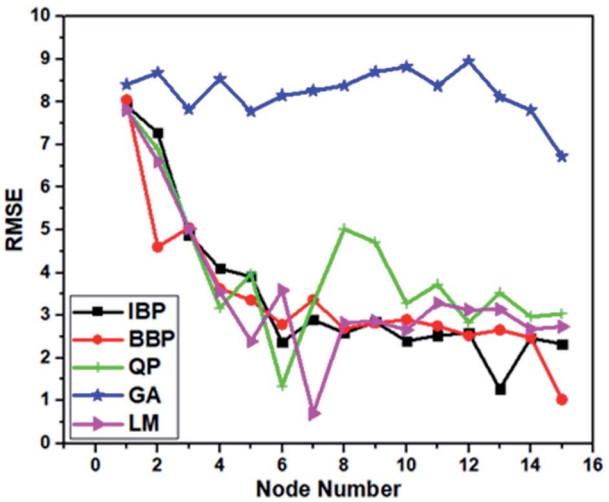

Fig. 1 The chosen RMSE *versus* node number of mean specific surface area of the NiO-ICG catalyst network's hidden layer for BBP, QP, IBP, GA, and LM.

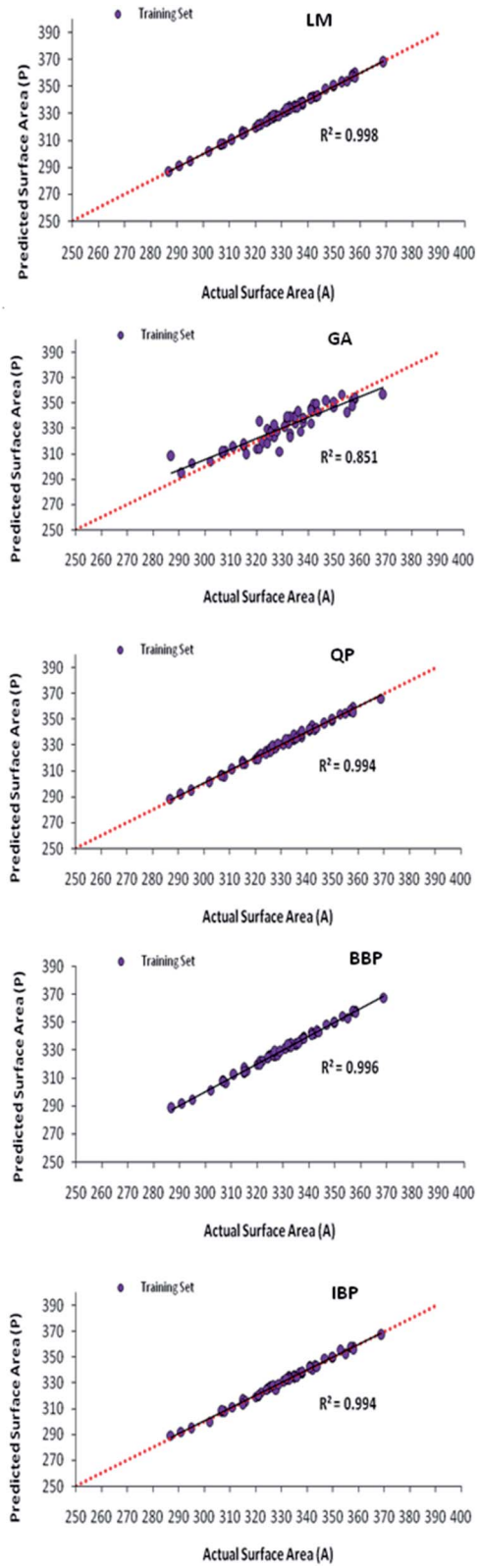

Fig. 2 The scatter plots of the forecasted specific surface areas against the actual crystal range for the training set of data for improved topologies of all the chosen algorithms.

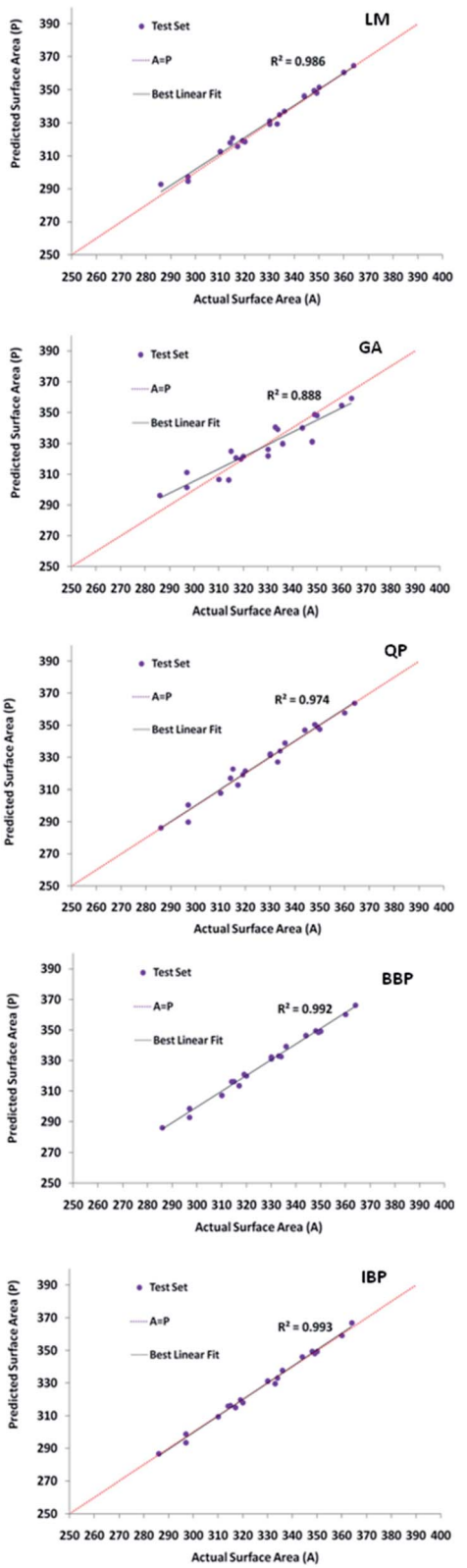

Fig. 3 The scatter plots of the forecasted specific surface areas against the testing data set for optimized topologies of all the selected algorithms.

where, C is the proportion of ester yield, $\sum A$ is the summation of the full area for the FFA peaks, A_{meh} is the peak area of the internal-standard, C_{meh} is the total loading of methyl heptadecanoate, V_{meh} is the total volume of methyl heptadecanoate, and W_t is the mass of the produced FAME.

Results and discussions

ANN modelling results

The topology of the algorithms. Fig. 1 demonstrates the RMSE *versus* node number of the mean specific surface area of the mesoporous network's hidden layer for BBP, QP, LM, IBP, and GA. The selected topologies for all the five algorithms were 4-6-1, 4-15-1, 4-13-1, 4-7-1, and 4-15-1 for QP, BBP, IBP, LM, and GA algorithms, respectively. Obviously, LM-4-7-1 was chosen as the optimum algorithm because it has the lowest RMSE value as the conditional version for the specific surface area of the mesoporous NiO-ICG nanocrystalline material. Therefore, the selected LM-4-7-1 model was further studied to choose a superior model.

Model selection. To verify the excellent model for the evaluation of specific surface area, the RMSE, R^2, and AAD values were determined comparatively among all the highlighted topologies. Fig. 2 depicts the actual and predicted values of specific surface areas for the training data. Similarly, the R^2 values for the training data were calculated, as shown in Fig. 3. It is evident that LM-4-7-1 topology had the maximum R^2 value of 0.986 for the testing set of data and 0.998 for the training outputs.

Moreover, the AAD values of the training and testing outputs for all the preferred topologies are summarized in Table 2. Evidently, LM-4-7-1 with the lowermost AAD value in the testing and training was preferred as the superior model because of possessing the highest R^2 value and the lowest RMSE and AAD values in comparison with others.

Validation of the model. The actual and predicted specific surface area values for the validation set of data for the selected LM-4-7-1 model are demonstrated in the scatter plot (see Fig. 4). As represented, the high R^2 value of 0.991 and low RMSE value of 2.405 and AAD value of 0.665 validated the ultimate analytical accuracy of the optimized pattern.

The network of the selected model. The schematic representation of the selected multilayer perception NN model for the specific surface areas of the mesoporous NiO-ICG catalyst is shown in Fig. 5. The selected model possessed three layers containing one input layer, one hidden layer, and one output layer. The four nodes of the input layer corresponded as the disseminator for the 6 nodes of the hidden layer, which was evaluated through the learning process.

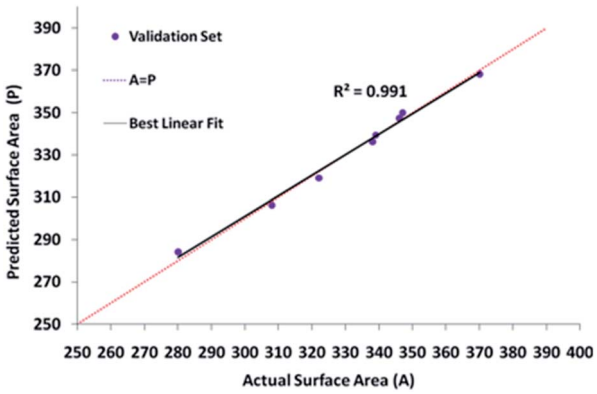

Fig. 4 The scatter plots of the predicted surface areas *versus* actual specific surface areas for validation set of data for the selected LM-4-7-1 model.

The graphical optimization. The selected network can help to navigate the specific surface area values of the synthesized NiO-ICG through graphical optimization of the important and effective elements. The selected LM-4-7-1 model was introduced in order to simulate the association between the chosen elements on the S_{BET} of the produced mesoporous NiO-ICG composite. In each three-dimensional (3D) plot format, the

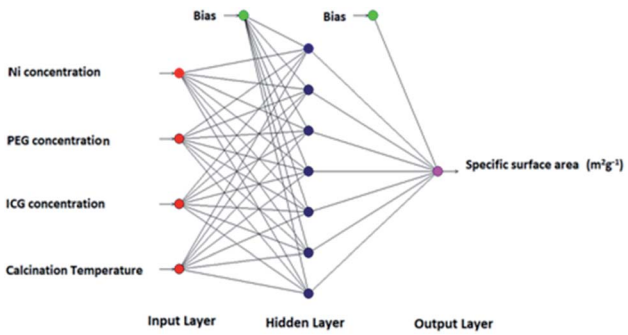

Fig. 5 Schematic representation of multilayer perception neural network.

Table 2 Improved topologies, QP-4-6-1, IBP-4-13-1, BBP-4-15-1, GA-4-15-1, and LM-4-7-1 on the specific surface area of the synthesized mesoporous NiO-ICG nanocrystalline material

		Training data set				Testing data set			
Learning algorithm	Architecture	RMSE	R^2	AAD	p value	RMSE	R^2	AAD	p value
QP	4-6-1	1.354	0.994	0.325	0.001	1.640	0.974	0.397	0.001
IBP	4-13-1	1.286	0.994	0.316	0.001	1.301	0.993	0.327	0.001
BBP	4-15-1	1.031	0.996	0.262	0.001	1.532	0.993	0.367	0.001
GA	4-15-1	6.722	0.851	1.605	0.001	7.413	0.888	1.826	0.001
LM	4-7-1	0.702	0.998	0.153	0.001	0.801	0.986	0.203	0.001

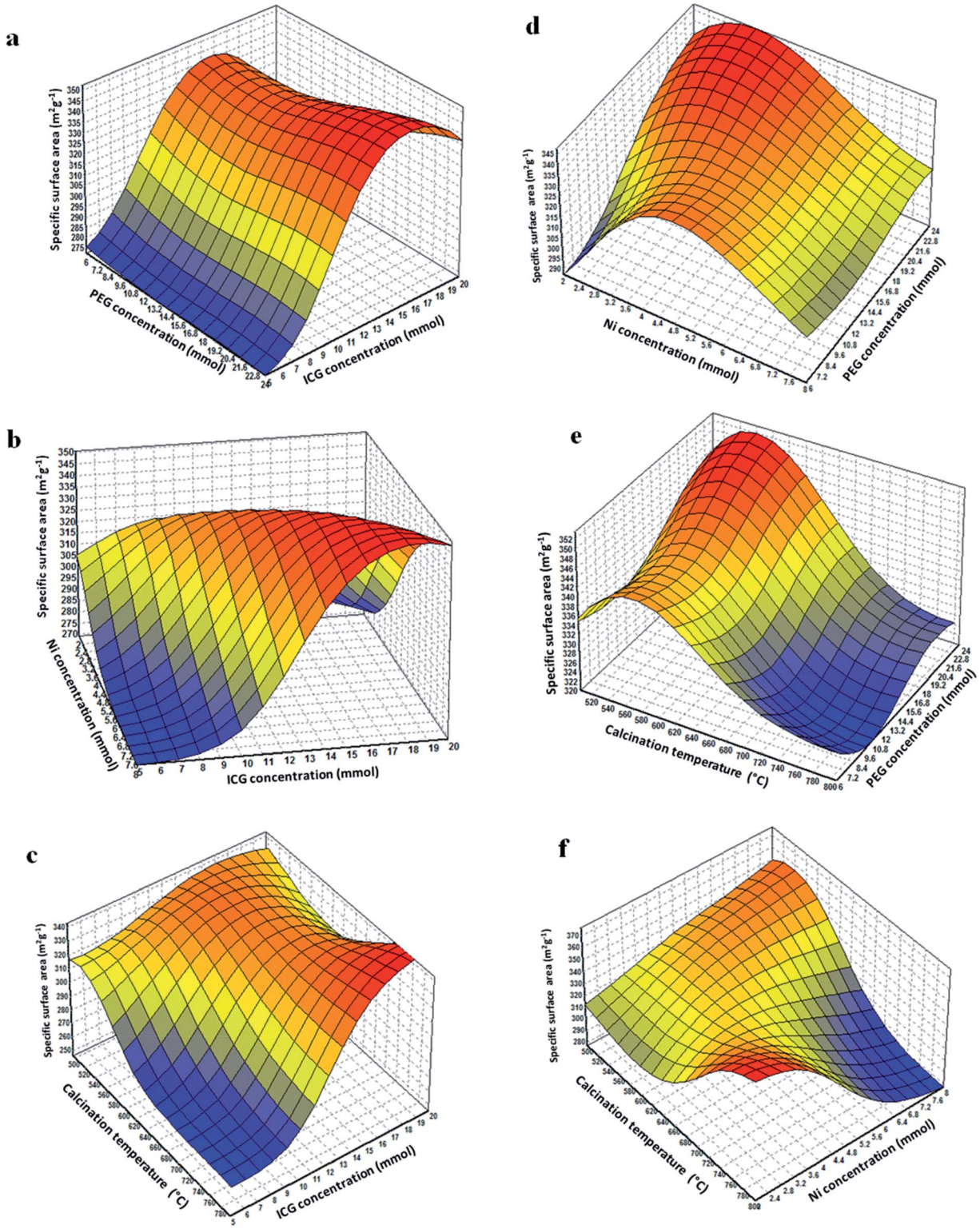

Fig. 6 The surface response of instantaneous impact of two variables on the specific surface area value of mesoporous NiO-ICG catalyst. (a) Correlation between PEG and ICG concentrations, (b) correlation between Ni and ICG concentrations, (c) correlation between ICG concentration and calcination temperature, (d) correlation between Ni and PEG concentrations, (e) correlation between calcination temperature and PEG concentration, (f) correlation between calcination temperature and Ni concentration, where the other two variables were retained untouched at the midpoint values in each plot.

Table 3 The alterations between the actual and the model-predicted specific surface area value of the mesoporous NiO-ICG composite

	ICG con. (g)	PEG con. (g)	Ni con. (mmol)	Calcination temp. (°C)	Actual surface area (m^2 g^{-1})	Predicted surface area (m^2 g^{-1})	Error (%)
Optimized variable	15	12	6	600	351	317.8	9.45

non-linear interaction between two different elements *versus* the specific surface area value is graphically represented in Fig. 6 whereas two more variables remained untouched at the midpoint values in each plot. In the present study, the canonical middle point for Ni concentration, PEG concentration, ICG concentration, and calcination temperature was 6 g, 12 g, 10 g, and 600 °C, respectively.

Fig. 6(a) illustrates the connections between the ICG ratio and PEG concentration. As shown, by increasing the ICG concentration from 0 to 16, the surface area increased while by further increasing the concentration from 16 to 20, the surface area decreased while the surface area was constant on increasing the PEG concentration.

Fig. 6(b) presents the interaction between two variables of ICG concentration and Ni concentration. As observed, the surface area was increased by increasing the ICG concentration, while the surface area decreased by increasing the Ni concentration.

Fig. 6(c) illustrates the interactions area of calcination temperature and ICG concentration. As presented, the surface area was increased by increasing the ICG concentration, while the surface area decreased by increasing the calcination temperature.

Fig. 6(d) shows the interactions between PEG concentration and Ni concentration. It was observed that by increasing the Ni concentration from 0 to 4, the surface area was increased while by further increasing the concentration from 4 to 8, the surface area decreased. The highest S_{BET} of the 3D plot was obtained at higher strengths of PEG and low concentrations of Ni (at about 3 mmol).

Fig. 6(e) demonstrates the 3D plot of PEG concentration against the calcination temperature. As demonstrated, higher S_{BET} was obtained using the low calcination temperature and high PEG concentration.

Fig. 6(f) illustrates the interactions between the Ni concentration and calcination temperature. By expanding the quantity of Ni, the S_{BET} decreased, whilst by rising the calcination temperature, the S_{BET} improved.

Table 3 indicates the alterations in the actual and the model-predicted S_{BET} of the NiO-ICG over the predicted optimum condition. Noticeably, the actual specific surface area was fairly near to the predicted value by means of the model with 9.45% miscalculation.

Importance of effective parameters. The percentage of significance of metal ratio, surfactant and template concentrations, and post-annealing temperature on the S_{BET} value of the authenticated model is illustrated in Fig. 7. Accordingly, the calcination temperature with a virtual efficiency of 29.97% showed the most effectual influence on the specific surface area value while the other parameters such as Ni and PEG concentrations also had extensive effects. It is worthy to mention that all the variables had their specific and typical importance.

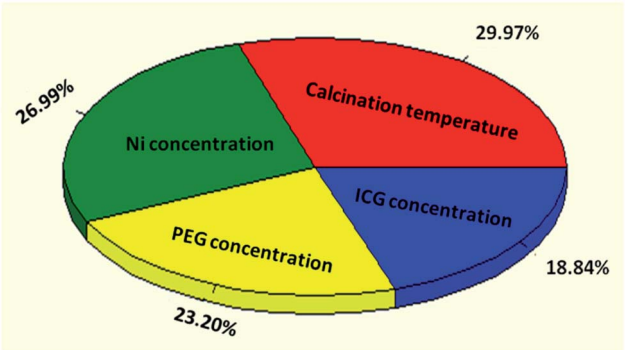

Fig. 7 The percentage significance of metal ratio, surfactant and template concentrations, and calcination temperature on the specific surface area value.

Proposed strategy of NiO heterogeneous sphere fabrication

The mechanism designed for the formation C@Ni core–shell solids using PEG-assisted method is displayed in Fig. 8. The

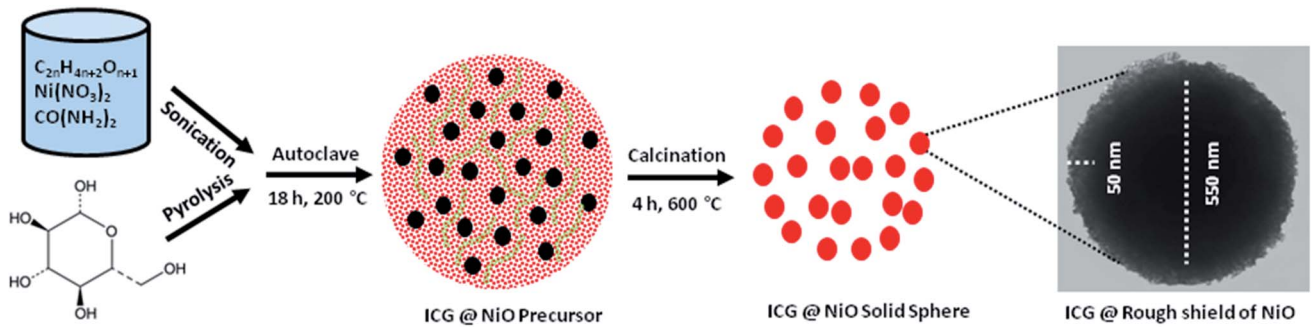

Fig. 8 Graphic illustration of the development of C@Ni using autoclave-assisted method including TEM image of the C@Ni solid-spheres.

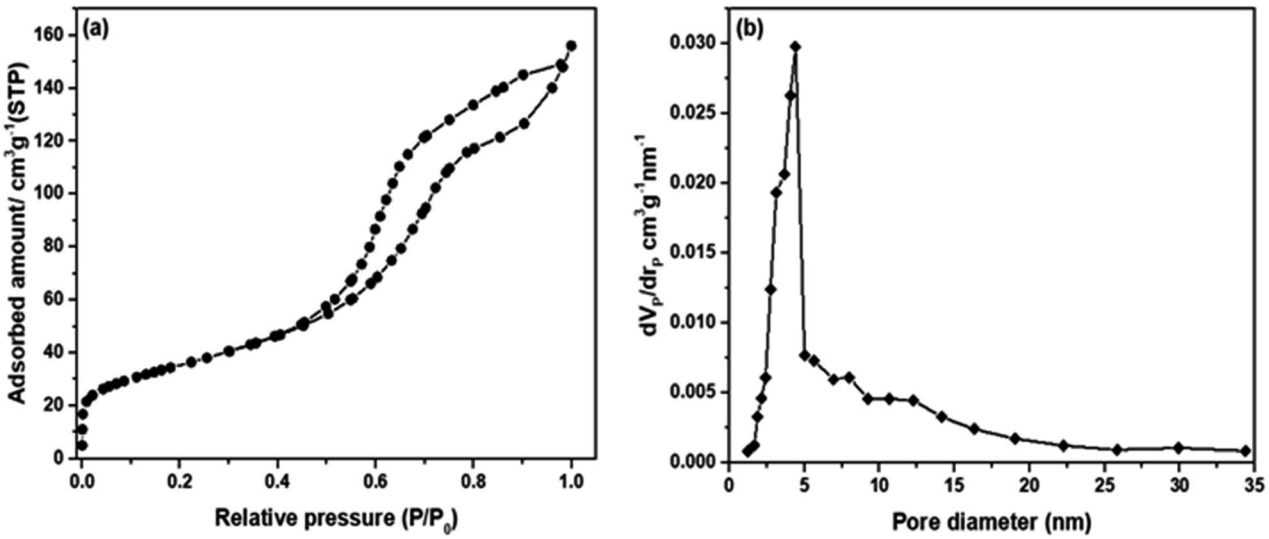

Fig. 9 (a) Nitrogen adsorption–desorption isotherms of the synthesized mesoporous NiO-ICG material and (b) pore size distribution determined by BJH method.

formation and development of C@Ni core–shell solid spheres occurred over a sequence of the following reaction steps in a Teflon-lined stainless-steel autoclave:[36,37]

$$n\mathrm{Ni(NO_3)} \rightarrow n\mathrm{Ni^{2+}} + [\mathrm{NO_3}]_{2n} \quad \text{(I)}$$

$$n\mathrm{Ni^{2+}} + \mathrm{OH^-} \rightarrow \mathrm{NiOH^-} \quad \text{(II)}$$

$$\mathrm{NiOH^-} \rightarrow \mathrm{NiOH} + \mathrm{e} \quad \text{(III)}$$

$$\mathrm{NiOH} + \mathrm{OH^-} \rightarrow \mathrm{Ni(OH)_2} + \mathrm{e} \quad \text{(IV)}$$

$$[\mathrm{Ni(OH)_2}]_n + n\mathrm{PEG} \rightarrow [\mathrm{Ni(OH)_2{-}PEG}]_n \quad \text{(V)}$$

Under autoclave reaction restrictions (high temperature high pressure) the ICG as the carbon source decomposed to the gassy composites (H_2, CO, and CO_2). These compounds further functioned as templates to build up primary spheres. Along with the formation carbonaceous spheres, the nickel nitrate decomposed to Ni^{2+} cation, which electrostatically interacted with –OH (hydrophilic species) to form the structure $Ni(OH)_2$ (steps (I)–(III)). As time went by, a complex compound of $[Ni(OH)_2]_n$ formed as the neighbouring $Ni(OH)_2$ and interacted together *via* hydrophilic species (steps (IV)). Next, the oxygen atoms of PEG components basically adsorbed at the positive charge of $Ni(OH)_2$ through H_2 bonding to develop chains of $[Ni(OH)_2–PEG]_n$ (step (V)). Basically, PEG adsorbed on the exterior layer of the particles as a result of water-soluble extended connection and hindered the adhesion and agglomeration of metal particles. At 200 °C, $Ni(OH)_2$ transformed into NiO, which further interacted and was incorporated into the carbon sphere surrounded by a shell of NiO nanoparticles placed at the outer surface of the carbonaceous core walls. Next, the post-annealing process was carried out to transform the C@Ni architecture into a mesoporous structure over nitrogen flow, which ultimately led to the formation of a soft shell of NiO nanoparticles around the carbonaceous core walls. As illustrated in Fig. 8, the low intensification TEM picture reveals the development of a noticeable core sphere with a diameter of about 550 nm and shell structure with a diameter of about 50 nm. The NiO shield and ICG nucleus were indicated in grey and black colours, respectively.

Catalyst characterization

The N_2 ads–des isotherm and pore size distribution of the produced mesoporous SO_3H–NiO-ICG are demonstrated in Fig. 9. The N_2 ads–des isotherm was characteristic of type IV according to the BDDT isotherm classification, which confirmed the mesoporous structure of the fabricated catalyst.[31]

Table 4 The textural characteristics of the proposed mesoporous NiO-ICG and SO_3H–NiO-ICG catalyst

Sample	S_{BET}[a] ($m^2\ g^{-1}$)	D_p[b] (nm)	V_p[c] ($cm^3\ g^{-1}$)	Crystallite size[d] (nm)
Optimized NiO-ICG	351.15	4.40	0.36	34.14
SO_3H–NiO-ICG	335.30	3.25	0.26	40.50

[a] Specific surface area were obtained from Brunauer, Emmett and Teller method. [b] Average pores size was calculated from the N_2 desorption branch using the BJH model. [c] Total pore volumes were calculated at $P/P_o = 0.99$ on the N_2 adsorption isotherms. [d] Average crystallite size were calculated from the values of FWHM of the (200) diffraction peak from the Scherrer equation.

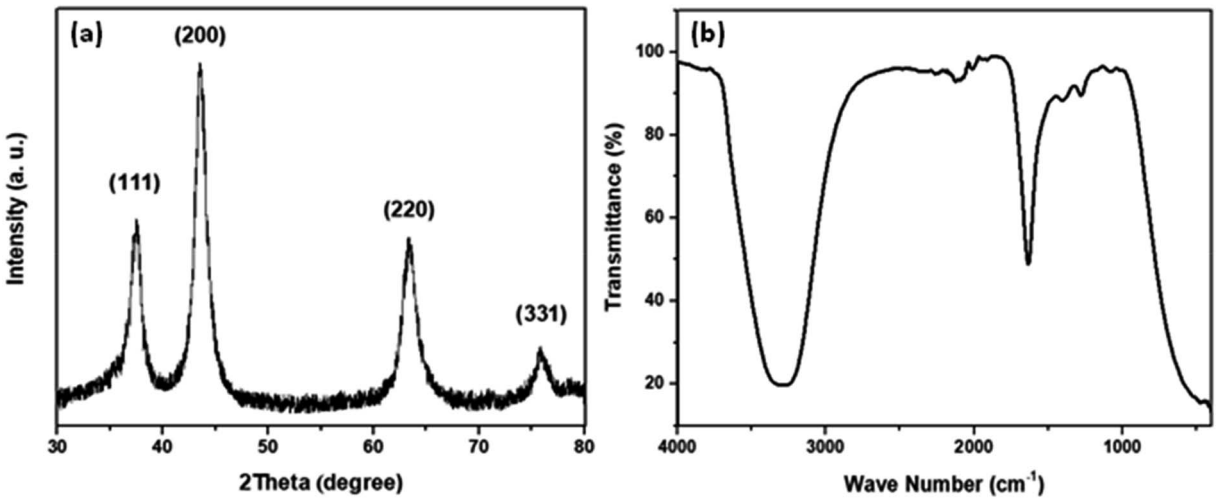

Fig. 10 (a) XRD pattern and (b) FT-IR spectra of the synthesized NiO-ICG composites.

The N_2 ads–desorption isotherm shows a weak and strong N_2 adsorption at $P/P_o < 0.4$ and $P/P_o > 0.4$, respectively (see Fig. 9(a)), which confirmed the formation of mono-modal mesopore diameter distribution.

Fig. 9(b) also evidenced the mono-modal mesopore diameter distribution with a sharp bow at 4.40 nm. The textural characteristics of the NiO-ICG catalyst are presented in Table 4.

The average crystal size of the synthesized NiO-ICG was evaluated using XRD. As demonstrated in Fig. 10, the X-ray peak reflections of (111), (200), (220), and (331) were detected at 37.45°, 43.66°, 63.50°, and 75.75°, respectively, which were associated with the cubic-phase NiO nanoparticles (JCPDS: #47-1049). The degree of crystallinity of the optimized NiO-ICG was measured with the Scherrer's formula:

$$D = 0.98\lambda/\beta \cos \theta_\beta$$

where D is the crystallite dimension (average), λ is the wavelength, β is the values of full width half maximum of the peaks, and θ_β is the Bragg-angle. According to the calculations, NiO-ICG had a crystallinity of about 34.14 nm.

The purity of NiO-ICG was verified by EDX analysis (Fig. 11), where atomic-ratios of Ni = 4.47, C = 50.32, and O = 45.21 were identified, which were according to the accurate stoichiometry of the elemental ratios and applied through the fabrication procedure.

After verifying the optimum hydrothermal conditions, TDAS was applied to attach $-SO_3H$ species to the active sites of the as-prepared materials. According to the TPD result, the mesoporous SO_3H–NiO-ICG catalyst possessed NH_3 acidity of 3.50 mmol g^{-1}.

The post-sulfonation temperature got a considerable impression on the textural properties where the surface area and porosity reduced to 335.30 m^2 g^{-1} and 3.25 nm, respectively. It is

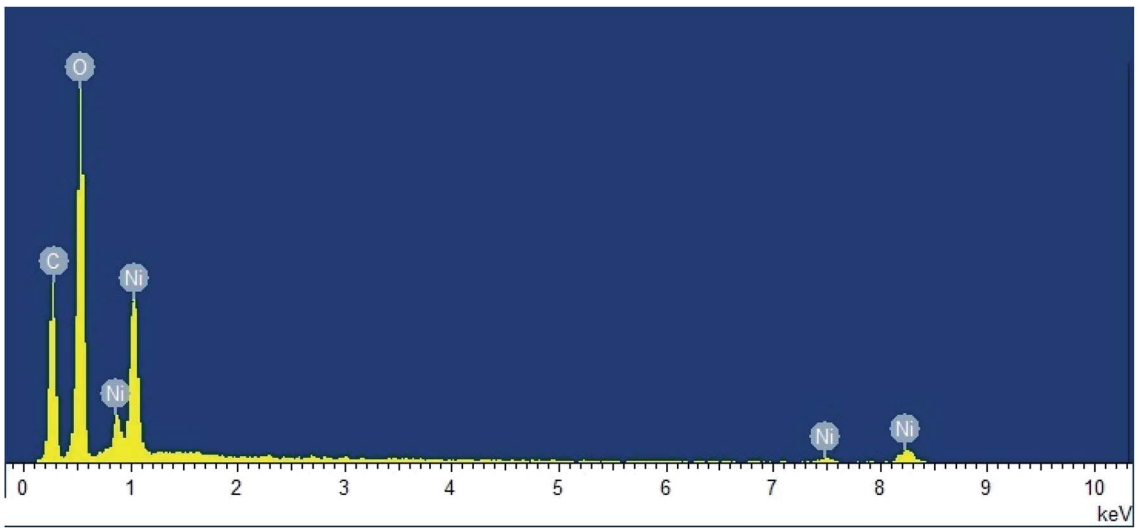

Fig. 11 EDX spectrum of the synthesized mesoporous NiO-ICG catalyst.

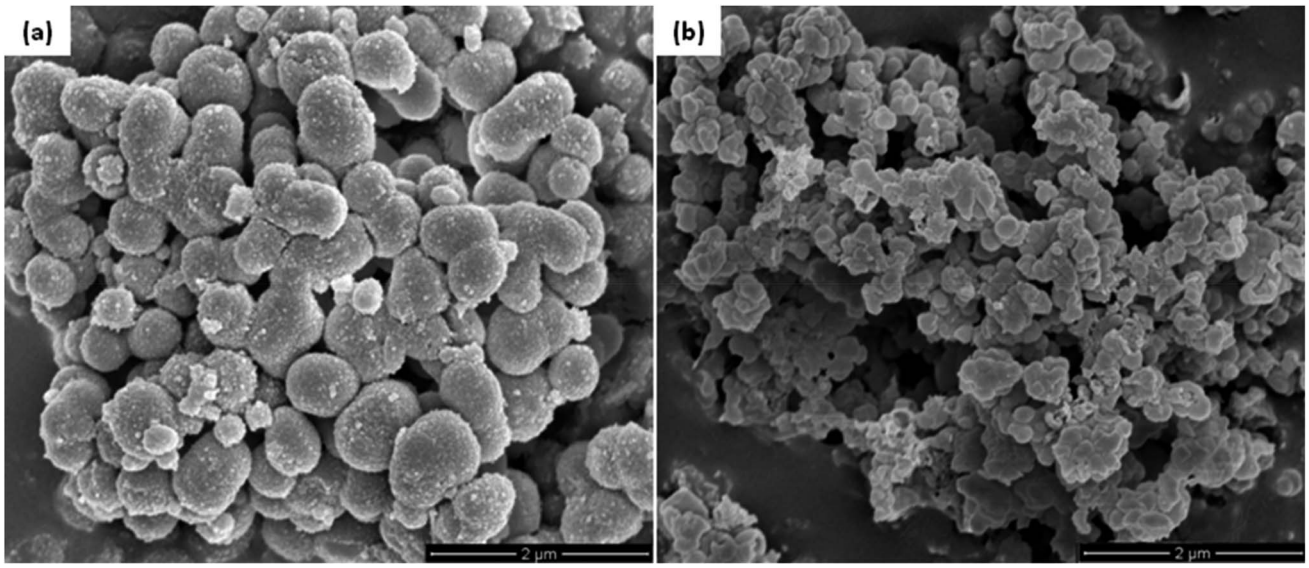

Fig. 12 FESEM images of (a) the synthesized NiO-ICG composites and (b) the mesoporous SO_3H–NiO-ICG catalyst.

worthy to mention that, however, the pores size sharply dropped and the mesostructured framework was preserved, which was corresponding to the unsuccessful bonding of sulfonic compounds at the inner pores of the surface.

The morphology of NiO-ICG and SO_3H–NiO-ICG composites was evaluated by FESEM image, as shown in Fig. 12(a). The formation of carbonaceous spheres with a rough shield of NiO nanocrystalline is confirmed. Fig. 12(b) shows the morphology of mesoporous SO_3H–NiO-ICG catalyst. It proved that the core–shell solid sphere structure slightly deformed after post-treatment.

Methyl ester production

Furthermore, the catalytic performance of the SO_3H–NiO-ICG catalyst was determined *via* transesterification of WCPO using an autoclave under the optimized conditions: the mesoporous catalyst amount of 1 wt%, methanol to oil molar ratio of 9 : 1, temperature of 100 °C, and mixing intensity of 450 rpm. The high FAME yield of was 97.4% achieved in the presence of the produced catalyst.

The catalytic solidity of the produced catalyst was further determined (see Fig. 13). Accordingly, the spent catalyst showed superior performance for ten successive reaction cycles with inconsequential loss of activity. The fatty acid methyl ester content dropped from 97.4% to 77.7% after 10 successive transesterification reaction while the leaching of the sulfonic compounds was negligible (2.11% to 1.53%, as measured by a CHNS elemental analyser). The superior reusability of the SO_3H–NiO-ICG catalyst was associated largely with the S_{BET} of the catalyst where larger pore size gives better opportunity to sulfonic functional species to incorporate into the mesopore frameworks.[37–39]

Generally speaking, ANN as an effective quantifiable procedure was highly suitable for modelling the selected operative input variables (such as metal ratio, surfactant and template concentrations, and calcination temperature) to predict the mean of

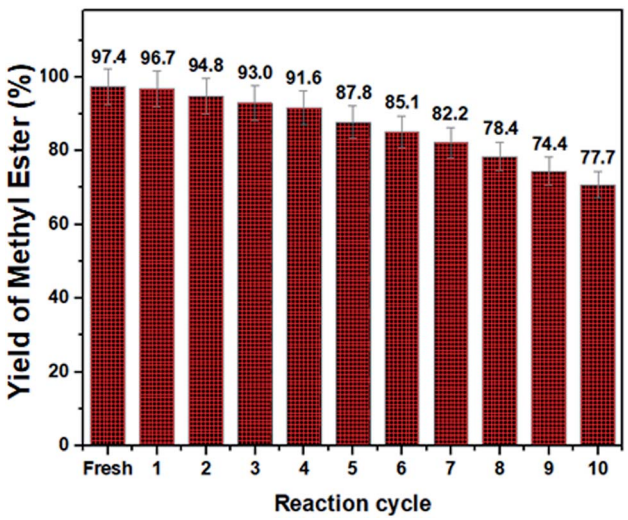

Fig. 13 Recyclability of SO_3H–NiO-ICG catalyst for ten runs under the optimal conditions: methanol to oil molar ratio, catalyst amount, reaction temperature, and mixing intensity of 9 : 1, 1.0 wt%, 100 °C, and 450 rpm, respectively.

surface area values of the synthesized mesoporous SO_3H–NiO-ICG catalyst. Furthermore, introducing ANN examination as an efficient numerical model would largely save the budget and time by foreseeing the outputs of the analytical procedure. In addition, it would highly ease the analytical procedure of the critical factors and their outcomes in complex systems.

Conclusion

Nanocrystalline mesoporous NiO-ICG core–shell solid sphere composites were successfully fabricated by hydrothermal

assisted method. The ANN method was applied to predict the specific surface area based on the input variables including metal ratio, surfactant and template concentrations, and calcination temperature. Among the four selected effective parameters, the calcination temperature with a relative efficiency of 29.97% was found to be the most effective variable on the surface area values. Noticeably, the actual specific surface area was fairly near to the predicted value by means of the model with an error of 9.45%. After verifying the optimum hydrothermal conditions, thermal decomposition of ammonium sulphate was applied to attach $-SO_3H$ functional groups to the active sites. The optimized NiO-ICG composite possessed unique structural and textural properties such as S_{BET} of 351.15 $m^2\ g^{-1}$, average D_p of 4.40 nm, total V_p of 0.36 $cm^3\ g^{-1}$, and crystallinity of 34.14 nm. Furthermore, the catalytic activity and recyclability of the SO_3H–NiO-ICG catalyst were determined *via* transesterification of WCPO. The high FAME yield of 97.4% was attained in the presence of the SO_3H–NiO-ICG catalyst while the spent catalyst showed superior catalytic activity for ten successive reaction cycles with inconsequential loss of activity.

Conflicts of interest

There are no conflicts to declare.

Acknowledgements

The authors would like to extend their profound gratitude to the Universiti Putra Malaysia (UPM) for the financial support for funding this research work through Geran Putra UPM GP-IPB/2016/9515200. The authors acknowledge their appreciation to King Saud University (Riyadh, Saudi Arabia) for the support of this research through Researchers Supporting Project number (RSP-2019/80). We also would like to convey the deepest gratitude and appreciation to Dr Maryam Shad for her ceaseless support.

Notes and references

1 V. B. Veljkovic, S. H. Lakicevic, O. S. Stamenkovic, Z. B. Todorovic and M. L. Lazic, *Fuel*, 2006, **85**, 2671–2675.
2 F. Guo, Z. Fang, C. C. Xu and R. L. Smith, *Prog. Energy Combust. Sci.*, 2012, **38**, 672–690.
3 T. Wagner, S. Haffer, C. Weinberger, D. Klaus and M. Tiemann, *Chem. Soc. Rev.*, 2013, **42**, 4036–4053.
4 W. Li and D. Zhao, *Chem. Commun.*, 2013, **49**, 943–946.
5 S. Soltani, U. Rashid, S. I. Al-Resayes and I. A. Nehdi, Mesoporous Catalysts for Biodiesel Production: A New Approach, *Clean Energy for Sustainable Development*, Academic Press, 2017, pp. 487–506.
6 M. Dorraj, Y. Abdollahi, S. B. M. Said, M. F. B. M. Sabri, N. A. Sairi, W. P. Meng and E. Abouzari-lotf, *RSC Adv.*, 2015, **5**, 21384–21395.
7 A. R. Khataee and M. B. Kasiri, *J. Mol. Catal. A: Chem.*, 2010, **331**, 86–100.
8 Y. Abdollahi, A. Zakaria, A. H. Abdullah, H. R. Fard Masoumi, H. Jahangirian, K. Shameli, M. Rezayi, S. Banerjee and T. Abdollahi, *Chem. Cent. J.*, 2012, **6**, 88.
9 E. Maleki, O. Unal and K. R. Kashyzadeh, *Mater. Charact.*, 2019, **157**, 109877.
10 S. Mandal, P. V. Sivaprasad, S. Venugopal and K. P. N. Murthy, *Appl. Soft Comput.*, 2009, **9**, 237–244.
11 M. O. Shabani and A. Mazahery, *Appl. Math. Model.*, 2012, **36**, 5455–5465.
12 Y. Duan, L. Ma, H. Qi, R. Li and P. Li, *Mater. Charact.*, 2017, **129**, 353–366.
13 S. Shazwani, M. Basri, H. R. F. Masoumi, E. A. Malek and R. A. Karjiban, *PLoS One*, 2016, **11**, e0157737.
14 H. R. Fard Masoumi, M. B. Ahmad, K. Shameli, M. Basri and K. Kalantari, *Ecol. Eng.*, 2016, **91**, 249–256.
15 S. Shukla, U. Kumar, A. Prakash and V. K. Jain, *Nanotechnol. Environ. Eng.*, 2017, **2**, 6.
16 A. Alirezaie, S. Saedodin, M. H. Esfe and S. H. Rostamian, *J. Mol. Liq.*, 2017, **241**, 173–181.
17 D. Bas and I. H. Boyaci, *J. Food Eng.*, 2007, **78**, 846–854.
18 M. A. Akcayol and C. Cinar, *Appl. Therm. Eng.*, 2005, **25**, 2341–2350.
19 T. T. Dele-Afolabi, M. A. Azmah Hanim, M. Norkhairunnisa, S. Sobri, R. Calin and Z. N. Ismarrubie, *Mater. Charact.*, 2018, **142**, 77–85.
20 Y. Abdollahi, N. A. Sairi, S. B. M. Said, E. Abouzari-lotf, A. Zakaria, M. F. B. M. Sabri, A. Islam and Y. Alias, *Spectrochim. Acta, Part A*, 2015, **150**, 892–901.
21 M. G. Moghaddam, F. B. H. Ahmad, M. Basri and M. B. A. Rahman, *Electron. J. Biotechnol.*, 2010, **13**, 3–4.
22 M. A. Hussain, M. Shafiur Rahman and C. W. Ng, *J. Food Eng.*, 2002, **51**, 239–248.
23 A. M. Rashidi, M. Hayati and A. Rezaei, *Mater. Des.*, 2012, **42**, 308–316.
24 P. Shabanzadeh, N. Senu, K. Shameli and M. M. Tabar, *J. Chem.*, 2013, **2013**, 8–316.
25 H. R. F. Masoumi, M. Basri, A. Kassim, D. Kuang Abdullah, Y. Abdollahi and S. S. A. Gani, *J. Surfactants Deterg.*, 2014, **17**, 287–294.
26 Y. Abdollahi, N. A. Sairi, M. K. Aroua, H. R. F. Masoumi, H. Jahangirian and Y. Alias, *J. Ind. Eng. Chem.*, 2015, **25**, 168–175.
27 Y. Abdollahi, N. A. Sairi, S. B. M. Said, E. Abouzari-Lotf, A. Zakaria, M. F. B. M. Sabri, A. Islam and Y. Alias, *Spectrochim. Acta, Part A*, 2015, **150**, 892–901.
28 S. Soltani, N. Khanian, U. Rashid and T. S. Y. Choong, *RSC Adv.*, 2019, **9**, 31306–31315.
29 A. Ghaffari, H. Abdollahi, M. R. Khoshayand, I. S. Bozchalooi, A. Dadgar and M. Rafiee-Tehrani, *Int. J. Pharm.*, 2006, **327**, 126–138.
30 D. Salari, N. Daneshvar, F. Aghazadeh and A. R. Khataee, *J. Hazard. Mater.*, 2005, **125**, 205–210.
31 S. Soltani, U. Rashid, T. R. Shojaei, I. A. Nehdi and M. Ibrahim, *Chem. Eng. Commun.*, 2019, **206**, 33–47.
32 E. Jorjani, S. C. Chelgani and S. H. Mesroghli, *Fuel*, 2008, **87**, 2727–2734.
33 J. Ren, R. Wang, Y. Feng, C. Peng and Z. Cai, *Mater. Charact.*, 2019, **156**, 109833.
34 H. N. Sin, S. Yusof, N. S. A. Hamid and R. A. Rahman, *J. Food Eng.*, 2006, **73**, 313–319.

35 L. Wang, B. Yang, R. Wang and X. Du, *Food Chem.*, 2008, **111**, 683–686.
36 S. Soltani, U. Rashid, R. Yunus and Y. H. Taufiq-Yap, *Fuel*, 2016, **178**, 253–262.
37 S. Soltani, U. Rashid, R. Yunus, Y. H. Taufiq-Yap and S. I. Al-Resayes, *Renewable Energy*, 2016, **99**, 1235–1243.
38 S. Soltani, U. Rashid, S. I. Al-Resayes and I. A. Nehdi, *J. Cleaner Prod.*, 2016, **144**, 482–491.
39 S. Soltani, U. Rashid, I. A. Nehdi and S. I. Al-Resayes, *Chem. Eng. Technol.*, 2017, **40**, 1931–1939.